PHYSICS

# On-chip integrated exceptional surface microlaser

**Kun Liao[1]†, Yangguang Zhong[2]†, Zhuochen Du[1]†, Guodong Liu[1], Chentong Li[1], Xianxin Wu[2], Chunhua Deng[3], Cuicui Lu[4], Xingyuan Wang[5], Che Ting Chan[6]*, Qinghai Song[3]*, Shufeng Wang[1,7,8]*, Xinfeng Liu[2]*, Xiaoyong Hu[1,7,8]*, Qihuang Gong[1,7,8]**



**The on-chip integrated visible microlaser is a core unit of high-speed visible-light communication with huge bandwidth resources, which needs robustness against fabrication errors, compressible linewidth, reducible threshold, and in-plane emission. However, until now, it has been a great challenge to meet these requirements simultaneously. Here, we report a scalable strategy to realize a robust on-chip integrated visible microlaser with further improved lasing performances enabled by the increased orders (*n*) of exceptional surfaces, and experimentally verify the strategy by demonstrating the performances of a second-order exceptional surface–tailored microlaser. We further prove the potential application of the strategy by discussing an exceptional surface–tailored topological microlaser with unique performances. This work lays a foundation for further development of on-chip integrated high-speed visible-light communication and processing systems, provides a platform for the fundamental study of non-Hermitian photonics, and proposes a feasible method of joint research for non-Hermitian photonics with nonlinear optics and topological photonics.**

## INTRODUCTION

The rapid development of mobile-internet and big-data services poses great challenges to the information capacity of communication networks. The standardization and industrialization of 5G/beyond 5G (B5G) communication technology (*1*–*7*) and the further proposal of B5G/6B communication architecture (*8*, *9*) have made high-speed visible-light communication technology one of the important parts of the wireless-communication blueprint owing to its low cost and large bandwidth. An on-chip integrated visible microlaser is a core unit of visible-light communication and information-processing systems and has four requirements: robustness against fabrication errors, a compressible linewidth, a reducible threshold, and in-plane emission with output light directly entering signal waveguides and photonic circuits (*10*, *11*). Representative implementation schemes for micro/nanolasers are summarized in Table 1 and detailed in table S1. We note that the table focuses on the capabilities and potentials of different micro/nanolaser schemes themselves in the mentioned performances rather than comparing the absolute value of performance indicators of different schemes.

Schemes for microlasers with novel physical phenomena tailored in non-Hermitian systems have been proposed (*12*–*14*), including those based on parity-time-symmetric microring lasers to select the desired parity-time (PT) symmetry breaking single mode (*15*–*19*), a single-cavity lasing on the isolated exceptional point (EP) by two Rayleigh scatterers when the relative angle is several special values (*20*, *21*), photonic molecules lasing at EP (*22*, *23*), and microcavity lasing with EP-tailored periodic complex index (*24*). Some of these non-Hermitian–tailored microlasers have the advantage of eliminating the undesired spatial hole-burning effect (*25*, *26*), which would improve the lasing efficiency, but without further discussion about simultaneous linewidth compression and threshold reduction. Moreover, schemes aiming to realize an isolated EP with strict and fragile degeneracy conditions usually require delicate parameter tuning of structures because of sensitivity to disturbance-like fabrication errors, which limits the performance of microlasers to a certain extent in terms of robustness and practicability.

Concerning other schemes for micro/nanolasers, plasmonic nanolasers have a compact footprint and a reduced threshold because of the strong light-confinement effect for plasmonic nanostructures, but they have a relatively broad linewidth (*27*–*29*). Although microlasers based on a bound state in the continuum (BIC) can reduce the threshold by exciting a leaky resonance formed by partially breaking a BIC in coupled nanopillars, they are short of linewidth compression and in-plane emission (*30*). BIC-based Fano microlasers can compress the lasing linewidth by forming a Fano resonance, but they are void of threshold reduction (*31*). Although topological vortex microlasers have good robustness when operating on a single spin momentum–locked edge mode, they are deficient in linewidth compression and in-plane emission (*32*). Last, silicon-organic hybrid microlasers meet the requirement of in-plane emission, but they lack linewidth compression and threshold reduction (*33*). Therefore, no existing microlaser scheme can meet the four requirements simultaneously for visible-light communication and information-processing systems.

[1]State Key Laboratory for Mesoscopic Physics and Department of Physics, Collaborative Innovation Center of Quantum Matter, Beijing Academy of Quantum Information Sciences, Nano-optoelectronics Frontier Center of Ministry of Education, Peking University, Beijing 100871, China. [2]CAS Key Laboratory of Standardization and Measurement for Nanotechnology, CAS Center for Excellence in Nanoscience, National Center for Nanoscience and Technology, Beijing 100190, China. [3]State Key Laboratory on Tunable laser Technology, Ministry of Industry and Information Technology Key Lab of Micro-Nano Optoelectronic Information System, Harbin Institute of Technology (Shenzhen), Shenzhen 518055, China. [4]Key Laboratory of Advanced Optoelectronic Quantum Architecture and Measurements of Ministry of Education, Beijing Key Laboratory of Nanophotonics and Ultrafine Optoelectronic Systems, School of Physics, Beijing Institute of Technology, Beijing 100081, China. [5]College of Mathematics and Physics, Beijing University of Chemical Technology, Beijing 100029, China. [6]Department of Physics, The Hong Kong University of Science and Technology, Clear Water Bay, Kowloon, Hong Kong, China. [7]Collaborative Innovation Center of Extreme Optics, Shanxi University, Taiyuan, Shanxi 030006, China. [8]Peking University Yangtze Delta Institute of Optoelectronics, Nantong, Jiangsu 226010, China.
†These authors contributed equally to this work.
*Corresponding author. Email: xiaoyonghu@pku.edu.cn (X.H.); liuxf@nanoctr.cn (X. L.); wangsf@pku.edu.cn (S.W.); qinghai.song@hit.edu.cn (Q.S.); phchan@ust.hk (C.T. C.)

**Table 1. Comparison between the exceptional surface (ES)–tailored microlaser and other implementation schemes for micro/nanolasers** QWs, quantum wells; MQWs, multiple quantum wells. "-" indicates that the property is not explicitly mentioned in the associated reference. RT, room temperature.

| Ref. | Scheme | | Gain material | Footprint | Wavelength | Temperature | Strong robustness | Threshold reduction | Linewidth compression | On-chip in-plane emission |
|---|---|---|---|---|---|---|---|---|---|---|
| **This work** | **ES-tailored microlaser** | | **$CsPbBr_3$** | **Diameter: 3 μm, MW:6 μm** | **~537 nm** | **RT** | **Yes (ES)** | **Yes (reduced to 44% compared with the control system)** | **Yes (compressed to 67% compared with the control system)** | **Yes (waveguide-coupled)** |
| (*15*) | PT-symmetric microring laser | Periodically gain/loss modulated single cavity | InGaAsP QWs | Diameter: 8.9 μm | ~1500 nm | RT | Yes | - | - | - |
| (*16*) | | Coupled resonators | InGaAsP QWs | ×2 Diameter: 20 μm | 1260–1600 nm | RT | Yes | - | - | - |
| (*20*) | EP-tailored laser | Rayleigh scatters tuned cavity | Erbium ions | Major diameter: 80 μm | ~1550 nm | RT | No | - | - | - |
| (*22*) | | Photonic molecules | InGaAsP QWs | ×3 Diameter: 20 μm | ~1600 nm | RT | No | No | No | - |
| (*24*) | | Complex index modulated cavity | InGaAsP MQWs | Diameter: 9 μm | ~1500 nm | RT | - | Yes | - | Yes |
| (*28*) | Plasmonic nanolasers | Localized SPR spaser | Dye | Diameter: 22 nm | 528 nm | RT | | - | Yes | - |
| (*29*) | | Plasmonic nanorod | InGaN/GaN | Diameter: ~40 nm, length: ~200 nm | 468–642 nm | 7 K | - | Yes | - | - |
| (*30*) | BIC laser | BIC nanopillar laser | GaAs nanopillars | ~55 μm × 90 μm | 825 nm | 77 K | Yes | Yes | - | No |
| (*31*) | | BIC-based Fano laser | InGaAsP QW | ~35 μm × 12 μm | 1560 nm | RT | Yes | No | Yes | Yes |
| (*32*) | Topological vortex laser | | InGaAsP MQWs | ~13 μm × 8 μm | ~1510 nm | RT | Yes | - | - | No |
| (*33*) | Silicon-organic hybrid laser | | IR26 polymer | ~3.8 mm × 575 nm | 1310 nm | RT | Yes | - | - | Yes |

Here, we report a scalable strategy to construct a robust on-chip integrated microlaser source with simultaneous in-plane emission, linewidth compression, and pump energy utilization improvement based on different orders of exceptional surfaces (ESs). In addition, all these excellent lasing performances are intrinsically derived from the tailoring of ESs rather than the simply engineering optimization. The configuration for the strategy consists of a gain-applied microcavity and an asymmetrically placed lossy modulation waveguide (MW) (a side-coupled straight waveguide below the microcavity or an unclosed ring in the microcavity). The MW induces asymmetrical reflection, leading to unidirectional emission in the microcavity, which is more robust and convenient to realize in experiments compared with accidental degeneracy schemes achieved by controlling Rayleigh scatterers (*21*) and constructing spiral or deforming microdisks (*34*, *35*). This emission is coupled to a transmission waveguide (TW). For demonstration, the configuration of a side-coupled straight waveguide below the microcavity is adopted in our experiments. Although the two ports of the MW act as reflectors, only the port of the short part of the MW can work effectively because of the material loss. As a result, one-way propagation of a traveling-wave mode can be obtained in the microcavity, ensuring the formation of the ES (*36*, *37*). The microlaser system is robust because the formation of the ES is insensitive to fabrication errors.

In our experiments, $CsPbBr_3$ perovskite is used as the gain/loss material (behaving as a lossy material in the absence of external pumping) because of its high optical-gain coefficient, low cost, and easy fabrication (*38*, *39*). The pumped microcavity, nonpumped MW, and TW are made of $CsPbBr_3$ perovskite to facilitate sample preparation. In a real photonic chip, the TW can be replaced with any low-loss dielectric waveguide. We experimentally demonstrate that a robust second-order ES-tailored microlaser has a laser linewidth of 0.8 nm and a pump threshold of 2.4 μJ/cm$^2$, which are simultaneously decreased to 67 and 44%, respectively, compared with those of a control system. Higher orders ($n$) of ES-tailored microlasers are also extended to be discussed here. The degree of linewidth compression and threshold reduction has a negative relation with $n$, and the degree of improved energy-conversion efficiency is proportional to $n$. Further discussion of an ES-tailored topological microlaser with a unique performance shows the superiority of our strategy. This work lays a foundation for further development of on-chip integrated high-speed visible-light communication and information-processing systems and opens research directions for non-Hermitian photonics with nonlinear optics and topological photonics.

## RESULTS

### System designed on a second-order ES

A schematic of the on-chip integrated microlaser is shown in Fig. 1A. The system consists of a microcavity with an intrinsic loss and applied gain, a coupled TW (with $s_1$ and $s_2$ specifying the amplitudes of the left and right ports, respectively), and a coupled MW (with amplitudes of $s_3$ and $s_4$ at the left and right ports, respectively) asymmetrically placed relative to the microcavity. Initially, two surrounding orientation modes, i.e., a clockwise (CW) mode and a counterclockwise (CCW) mode, are supported in the microcavity. In the ES configuration, the CW mode couples out from the microcavity and reflects from the short left port 3 of the MW. It subsequently couples back to the microcavity with a reversal of the surrounding orientation (the $CCW_{CW\ Reflected}$ mode), resulting in transfer from the CW mode to the $CCW_{CW\ Reflected}$ mode. The original CCW mode couples out from the microcavity and travels to the long right part of the lossy MW, i.e., the rare CCW component can be reflected in port 4 of this long right part. In this way, one-way propagation of the CCW traveling-wave mode is realized in the microcavity, making the system reach the ES.

Here, we analyze the performance of the proposed microlaser from a physical perspective of pump energy utilization between the two eigenmodes $|+\rangle$ and $|-\rangle$ in the microcavity. For the ES condition, the two eigenmodes degenerate with only the CCW component. In the control system (shown in Fig. 1B), the lossy MW is positioned symmetrically relative to the microcavity; i.e., the reflection coefficients at the left and right ports are equal and far less than 1. Only the eigenmode $|+\rangle$ with both CCW and CW components exists in the microcavity. It can be easily seen that the former system has less energy dissipation and thus higher energy utilization under the same pump power. Therefore, the spike generated in the lasing gets higher and narrower in the transmission spectrum at port 1 in the ES system, while the spike has a lower peak and wider linewidth in the transmission spectrum at both the left and right ports of the TW in the control system.

We used temporal coupled mode theory (TCMT) (*40*) to study properties of the system below the lasing regime

$$\frac{da_{cw}}{dt} = [i(\omega - \omega_0) - (\gamma_1 + \gamma_2 + \gamma_0 - g)]a_{cw} + 2\gamma_1\kappa_r e^{i\phi_r}a_{ccw} \quad (1)$$

$$\frac{da_{ccw}}{dt} = [i(\omega - \omega_0) - (\gamma_1 + \gamma_2 + \gamma_0 - g)]a_{ccw} + 2\gamma_1\kappa_l e^{i\phi_l}a_{cw} \quad (2)$$

where $a_{cw}$ and $a_{ccw}$ are the amplitudes of the CW and CCW traveling-wave modes in the microcavity, respectively; $\omega_0$ is the resonant frequency of the microcavity; $\gamma_1$ and $\gamma_2$ are the microcavity-MW and microcavity-TW coupling coefficients, respectively; $\gamma_0$ is the intrinsic loss of the microcavity; $g$ is the gain applied to the microcavity; and $\kappa_{l/r}$ and $\phi_{l/r}$ are the reflection coefficient and additional phase for the left/right side path of the MW. The Hamiltonian matrix of the system can be expressed as

$$H = \begin{bmatrix} \omega_0 - \omega - i(\gamma_1 + \gamma_2 + \gamma_0 - g) & -2i\gamma_1\kappa_r e^{i\phi r} \\ -2i\gamma_1\kappa_l e^{i\phi l} & \omega_0 - \omega - i(\gamma_1 + \gamma_2 + \gamma_0 - g) \end{bmatrix} \quad (3)$$

The eigenvalues and the corresponding eigenstates of the ES-tailored system can be written as

$$\begin{aligned} \omega_\pm &= \omega_0 - i(\gamma_1 + \gamma_2 + \gamma_0) \\ &\quad \mp 2\gamma_1\sqrt{\kappa_l\kappa_r}\exp\left[\frac{1}{2}i(\phi_l + \phi_r)\right], \vec{\alpha}_\pm \\ &= \frac{1}{\sqrt{\kappa_l^2 + \kappa_r^2}}(\pm\kappa_r, \kappa_l)^T \end{aligned} \quad (4)$$

For a diabolic surface (*41*, *42*) (i.e., when $\kappa_l = \kappa_r = 0$), the off-diagonal term of $H_{ES}$ is zero, the eigenvalues are coalesced, and the eigenmodes are orthogonal. For the ES condition (i.e., when $\kappa_l \gg \kappa_r$), the Hamiltonian matrix becomes the nondiagonalizable form

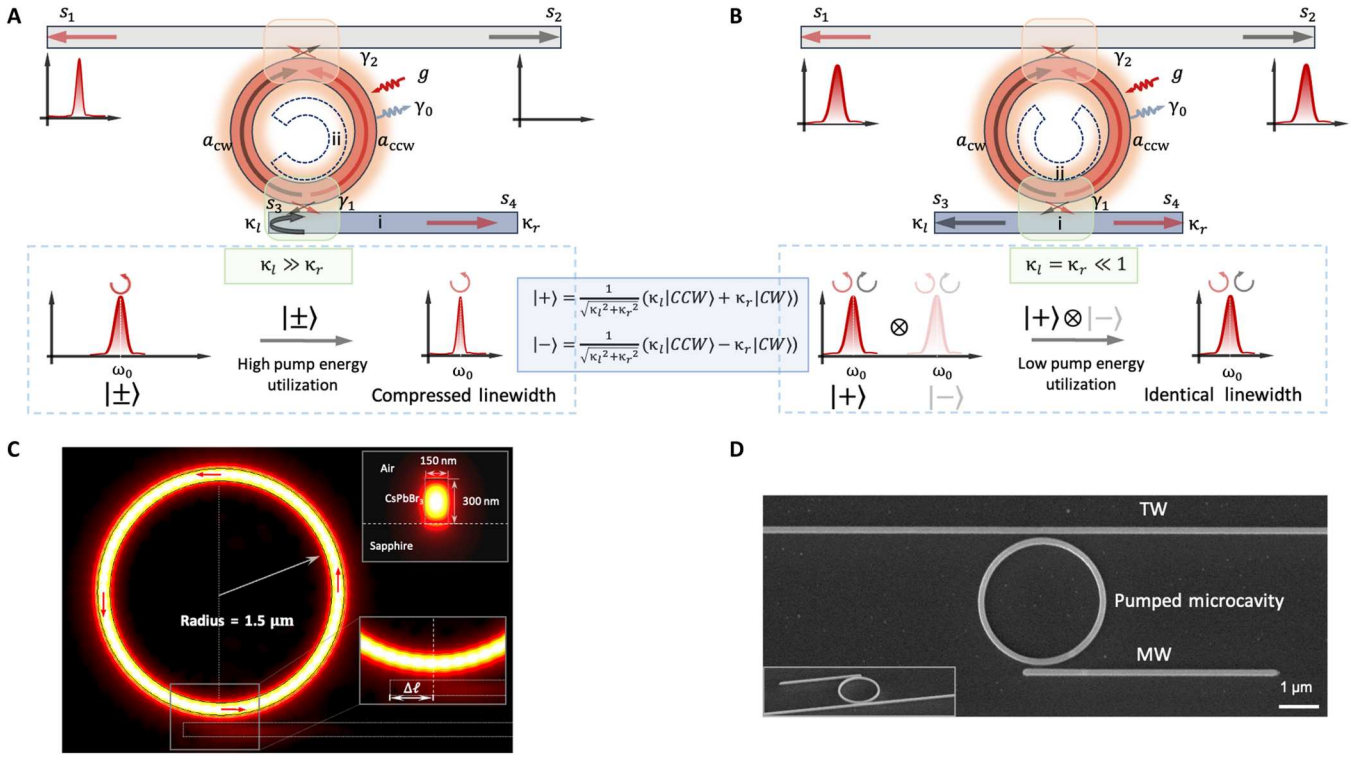


**Fig. 1. Strategy of the proposed exceptional surface (ES)–tailored microlaser system.** (**A**) Schematic diagram of the proposed system, which consists of a microcavity with an applied gain, a coupled transmission waveguide (TW), and a coupled modulation waveguide (MW) asymmetrically placed relative to the microcavity (configuration i and ii) with $\kappa_l \gg \kappa_r$ to realize one-way propagation of the counterclockwise (CCW) traveling-wave mode. A higher intensity and narrower linewidth in the transmission spectrum can be realized at port 1 by degenerate eigenmodes $|\pm|$ with only the CCW component. (**B**) Schematic diagram of the control system in which the MW is positioned symmetrically relative to the microcavity (configuration i and ii) with $\kappa_l = \kappa_r \leq 1$. Only the eigenmode $|+\rangle$ with both CCW and clockwise (CW) components exists in the microcavity. The lower peak and wider linewidth shown in the transmission spectrum at both the left and right ports of the TW are caused by more energy dissipation and thus lower energy utilization under the same pump power compared with the ES system. (**C**) Electric-field distribution of the eigenmode of the ES-tailored system obtained by eigenfrequency simulation (with a microcavity radius of 1.5 μm). The red arrows in the microcavity represent the time-averaged power outflow of the light field in the microcavity, indicating excellent one-way mode propagation. Bottom-right inset: Enlarged view of the microcavity-MW coupling area. Top-right inset: Simulation result for the mode distribution of the light field in the cross section of the $CsPbBr_3$ waveguide (width: 150 nm; height: 300 nm), which confines the light field well. (**D**) Top-view SEM image and tilted SEM image at 52° (inset) of the fabricated $CsPbBr_3$ microcavity-MW-TW coupled system. Scale bar, 1 μm.

with the coalesced eigenvalues and corresponding eigenstates

$$H_{\mathrm{ES}} = \begin{bmatrix} \omega_0 - \omega - i(\gamma_1 + \gamma_2 + \gamma_0) & 0 \\ -2i\gamma_1\kappa_l e^{i\phi_l} & \omega_0 - \omega - i(\gamma_1 + \gamma_2 + \gamma_0) \end{bmatrix} \tag{5}$$

$$\omega_{\pm} = \omega_0 - i(\gamma_1 + \gamma_2 + \gamma_0), \vec{\alpha}_{\pm} = (0,1)^T \tag{6}$$

It is clear from the matrix form of $H_{\mathrm{ES}}$ that the system is non-Hermitian and works on a hypersurface of EPs, where it is true for any values of $w_0$, $\gamma_1$, $\gamma_2$, $\gamma_0$, and $g$, making the system more robust against disturbances such as scattering of external scatterers and a shift of system parameters induced by a fabrication error compared with other non-Hermitian systems based on an isolated EP. The presence or absence of the off-diagonal term of $H_{\mathrm{ES}}$ depends only on the relative value of the two reflection coefficients at the left and right ports of the MW, and the diagonal terms are always the same because they refer to the same microcavity. Figure 2 (A and B) shows how the real and imaginary parts of the eigenvalues vary with the reflection-coefficient ratio of the left and right ports of the MW ($\kappa_l/\kappa_r$) and the associated parameter δ (donating the loss or gain of the microcavity, i.e., $\gamma_0$, $\gamma_1$, $\gamma_2$, and $g$). As the reflection-coefficient ratio increases, the real and imaginary parts of two eigenvalues gradually coalesce and remain in this state. Unlike a system with an accidental degenerate point, as long as the ratio is large enough, the proposed system will always remain in the second-order ES condition.

To better understand the performance of the proposed system without active gain, we theoretically calculated the transmission and reflection spectra for both ES and the control system (*43*). Here, we have

$$\frac{d}{dt}\begin{bmatrix} a_{\mathrm{cw}} \\ a_{\mathrm{ccw}} \end{bmatrix} = -iH_{\mathrm{CS/ES}}\begin{bmatrix} a_{\mathrm{cw}} \\ a_{\mathrm{ccw}} \end{bmatrix} + \sqrt{2\gamma_2}\begin{bmatrix} s_l \\ s_r \end{bmatrix} = 0 \tag{7}$$

Here, $s_l$ and $s_r$ represent the input from the left and right port of TW, respectively. In the control system, $\kappa_l = \kappa_r \ll 1$,there is no coupling between CW and CCW mode, so the reflection $R_l$ and $R_r$ are always 0. The transmission of the two ports is $T_l = T_r = \frac{|s_l - \sqrt{2\gamma_2}a_{\mathrm{cw}}|^2}{s_l^2} = \frac{(\omega-\omega_0)^2+(\gamma_0+\gamma_1-\gamma_2)^2}{(\omega-\omega_0)^2+(\gamma_0+\gamma_1+\gamma_2)^2}$, which shows a Lorentzian profile. For the ES system, $T_r$, $T_l$, and $R_r$ remain the same as the

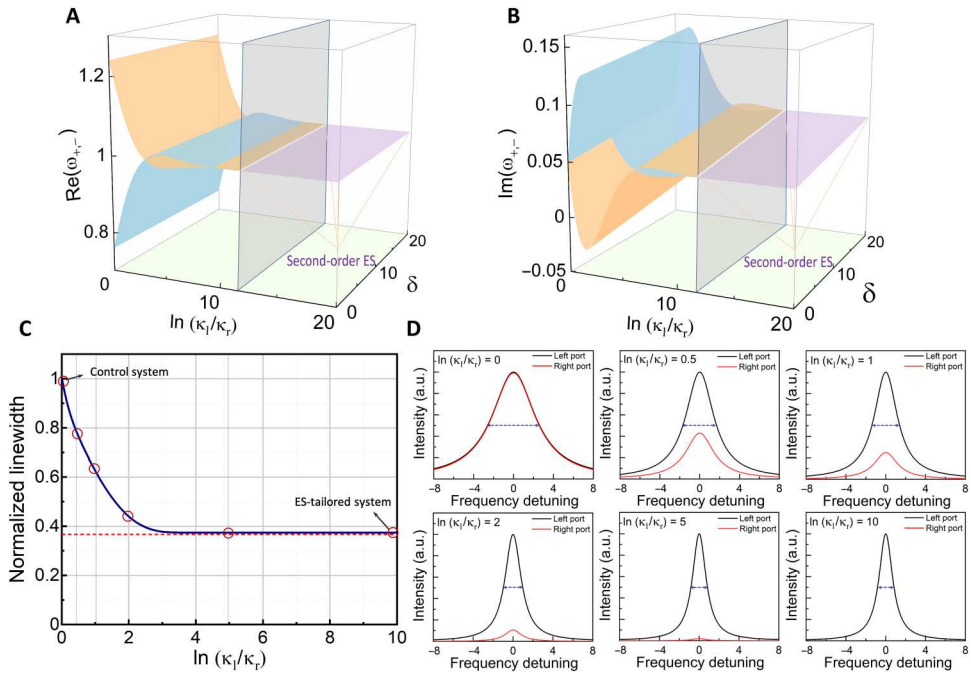


**Fig. 2. Theoretical characterization of key features of the proposed second-order exceptional surface (ES)–tailored microlaser.** (**A** and **B**) Real and imaginary parts of the eigenvalues of the system varying with the reflection-coefficient ratio of the left and right ports of the modulation waveguide (MW) ($\kappa_l/\kappa_r$) and the associated parameter δ (donating the loss or gain of the microcavity, i.e., $\gamma_0$, $\gamma_1$, $\gamma_2$, and *g*), showing that the system works on a hypersurface of second-order exceptional points (EPs). As long as the ratio is large enough, the system remains on the ES. (**C**) Normalized intrinsic laser linewidth at port 1 versus ln($\kappa_l/\kappa_r$). The linewidth has a maximum initial value of when $\kappa_r = \kappa_l$ (corresponding to the control system) and converges to 37% when $\kappa_l \gg \kappa_r$ in the ES-tailored system. (**D**) Transmission spectrum as a function of the frequency detuning when ln($\kappa_l/\kappa_r$) is 0, 0.5, 1, 2, 5, and 10, respectively, which can clearly describe the change of the laser linewidth with the reflection-coefficient ratio. a.u., arbitrary units.

control system. However, the reflection spectrum changes when the input light comes from the left port of TW, $R_l = \frac{4\gamma_1^2\kappa_l^2}{[(\omega-\omega_0)^2+(\gamma_0+\gamma_1+\gamma_2)^2]^2}$, which shows a squared-Lorentzian profile.

However, the TCMT alone is not sufficient to discuss a lasing system. When the external pumping is above the lasing threshold, we need to modify the equation (i.e., we consider the saturation effect and phase-amplitude coupling, etc.) to describe the dynamic evolution of the lasing amplitude by introducing the Lamb equation (*44*, *45*)

$$\frac{d}{dt}E_{cw(ccw)} = (1+i\alpha)[-(\gamma_0+\gamma_1+\gamma_2)+g(1-S|E_{cw(ccw)}|^2 - C|E_{ccw(cw)}|^2)]E_{cw(ccw)} - 2i\gamma_1\kappa_{r(l)}e^{i\phi_{r(l)}}E_{ccw(cw)} \quad (8)$$

To avoid confusion, here, we used $E_{cw}$ and $E_{ccw}$ to represent the electric field of the CW and CCW traveling-lasing-wave modes. We have $E_{cw(ccw)} = |E_{cw(ccw)}|e^{-i\omega t + i\phi_{cw(ccw)}}$, where ω is the lasing frequency and $\phi_{cw(ccw)}$ is the time-dependent phase factor. *g* is the gain coefficient originating from the external pumping. α accounts for the phase-amplitude coupling. *S* and *C* are self- and cross-saturation coefficients, respectively. We can also write down the dynamic equation of the inversion number *N*

$$\frac{d}{dt}N = v - v_0N - v_0N(1-S|E_{cw}|^2 - C|E_{ccw}|^2)|E_{cw}|^2 - v_0N(1-S|E_{ccw}|^2C|E_{cw}|^2)|E_{ccw}|^2 \quad (9)$$

where *v* is the time averaged pump rate and $v_0$ is the spontaneous emission (SE) rate. We mainly focus on the steady-state solution of these nonlinear equations, namely, $\frac{d}{dt}E_{cw(ccw)} = 0$ and $\frac{d}{dt}N = 0$. The output intensity at port 1 and port 2 of the TW, which is proportional to $|E_{ccw}|^2$ and $|E_{cw}|^2$, can be numerically derived under steady-state conditions. For the control system, the coupling between CW and CCW mode is symmetric. By using Sorel's method (*46*), we found that our assumed symmetric solution is stable in the control system. Here, we have

$$|E_{cw}|^2 = |E_{ccw}|^2 = \frac{2k(\gamma_0+\gamma_1+\gamma_2)+v(S+C)-\sqrt{[2k(\gamma_0+\gamma_1+\gamma_2)+v(S+C)]^2-8[v-v_0(\gamma_0+\gamma_1+\gamma_2)]\kappa(S+C)(\gamma_0+\gamma_1+\gamma_2)}}{4k(S+C)(\gamma_0+\gamma_1+\gamma_2)} \quad (10)$$

For the ES system, we found that the amplitude for CW mode should be zero to meet the stable condition. Thus, we have

$$|E_{cw}|^2 = 0,\ |E_{ccw}|^2 = \frac{vS+k(\gamma_0+\gamma_1+\gamma_2)-\sqrt{[vS+k(\gamma_0+\gamma_1+\gamma_2)]^2-4[v-v_0(\gamma_0+\gamma_1+\gamma_2)]\kappa S(\gamma_0+\gamma_1+\gamma_2)}}{2Sk(\gamma_0+\gamma_1+\gamma_2)} \quad (11)$$

We then analyzed the stability of these solutions also from the Lamb equation. We considered a perturbation for the electric field (for example, the SE noise) and the inversion number. Hence, the total electric field can be written as $E = E_{st} + \Delta E$, where $E_{st}$ means the steady-state solution for electric field and $\Delta E$ represents the perturbation. Similarly, we have $g = g_{st} + \Delta g$. We

ignored the second- and higher-order term such as $(\Delta E)^2$, $(\Delta g)^2$, $(\Delta E \Delta g)$, etc., in the Lamb equation, and we get

$$\frac{d}{dt}\Delta E_{cw(ccw)} = \Delta g(1 - S|E_{cw(ccw)}|^2 - C|E_{ccw(cw)}|^2)(1 + i\alpha)E_{cw(ccw)} - 2g(SE^*_{cw(ccw)}\Delta E_{cw(ccw)} + CE^*_{ccw(cw)}\Delta E_{ccw(cw)} + c.c.)E_{cw(ccw)} \quad (12)$$

$$\begin{aligned}\frac{d}{dt}\Delta N = &-\nu\Delta N - 2\nu_0 N(1 - S|E_{cw}|^2 - C|E_{ccw}|^2)(E^*_{cw}\Delta E_{cw} + c.c.) \\ &- 2\nu_0 N(1 - S|E_{ccw}|^2 - C|E_{cw}|^2)(E_{ccw}\Delta E_{ccw} + c.c.) - \\ &\nu_0 N(-2SE^*_{cw}\Delta E_{cw} - 2CE^*_{ccw}\Delta E_{ccw} + c.c.)|E_{cw}|^2 - \\ &\nu_0 N(-2SE^*_{ccw}\Delta E_{ccw} - 2CE^*_{cw}\Delta E_{cw} + c.c.)|E_{ccw}|^2\end{aligned} \quad (13)$$

where "c.c." refers to complex conjugates. For simplicity, we write the above equation as

$$\frac{d}{dt}\begin{bmatrix}\Delta E_{cw}\\ \Delta E_{ccw}\\ \Delta E^*_{cw}\\ \Delta E^*_{ccw}\\ \Delta g\end{bmatrix} = A\begin{bmatrix}\Delta E_{cw}\\ \Delta E_{ccw}\\ \Delta E^*_{cw}\\ \Delta E^*_{ccw}\\ \Delta g\end{bmatrix} \quad (14)$$

The stable condition requires the real part of all eigenvalues of $A$ to be negative, which means that the perturbation decays exponentially with time. It is easy to calculate the solutions in both control system and the ES case to show that they are stable.

The squared-Lorentzian profile is characteristic of both the EP (*47*) and ES system (*43*, *48*). To further study the behavior of the system below the laser threshold, we calculated the power spectra of a single quantum emitter (QE) coupled to the microcavity. We added the excitation term $c_{cw}$ and $c_{ccw}$ in the TCMT to represent the QE emission. It is worth noting that we only considered the intrinsic loss (radiation loss of microcavity) and coupling loss; the imaginary part of the $CsPbBr_3$ perovskite–induced propagation loss in microcavity will not be considered in this part. Here, we have

$$i\frac{d}{dt}\begin{bmatrix}a_{cw}\\ a_{ccw}\end{bmatrix} = H_{ES}\begin{bmatrix}a_{cw}\\ a_{ccw}\end{bmatrix} + \begin{bmatrix}c_{cw}\\ c_{ccw}\end{bmatrix} \quad (15)$$

Here, we set $|c_{cw}|^2 = |c_{ccw}|^2 = \eta(\phi)$, where $\eta(\phi)$ represents the relative Purcell factor ("relative" means we set $\eta \equiv 1$ in the control system) at azimuth angle $\phi$ (*49*) . The steady-state solution in the frequency domain is as follows

$$\begin{aligned}a_{cw} &= \frac{[\omega_0 - \omega - i(\gamma_0 + \gamma_1 + \gamma_2)]c_{cw} - 2i\gamma_1\kappa_r e^{i\phi_r}c_{ccw}}{[\omega_0 - \omega - i(\gamma_0 + \gamma_1 + \gamma_2)]^2 + 4\gamma_1^2\kappa_r\kappa_l e^{i(\phi_r+\phi_l)}},\ a_{ccw} \\ &= \frac{[\omega_0 - \omega - i(\gamma_0 + \gamma_1 + \gamma_2)]c_{ccw} - 2i\gamma_1\kappa_l e^{i\phi_l}c_{cw}}{[\omega_0 - \omega - i(\gamma_0 + \gamma_1 + \gamma_2)]^2 + 4\gamma_1^2\kappa_r\kappa_l e^{i(\phi_r+\phi_l)}}\end{aligned} \quad (16)$$

We have $\gamma_1 = \gamma_2$, and $\gamma_0 \ll \gamma_1 = \gamma_2$ in our numerical calculation. In the control system, the total output power in the frequency domain is $P_{CS} = 2(\gamma_1 + \gamma_2)\int_0^{2\pi}(|a_{cw}|^2 + |a_{ccw}|^2)d\phi = \frac{8\pi\gamma_1}{(\omega-\omega_0)^2+4\gamma_1^2}$, which shows a clearly Lorentzian spectra. As for the ES system, we have $P_{cw} = \int_0^{2\pi}|a_{cw}|^2 d\phi = \frac{4\pi\gamma_1}{(\omega-\omega_0)^2+4\gamma_1^2}$ and $P_{ccw} = \int_0^{2\pi}|a_{ccw}|^2 d\phi = \frac{[(\omega-\omega_0)^2+4\gamma_1^2]+4\gamma_1^2\kappa_l^2}{[(\omega-\omega_0)^2+4\gamma_1^2]^2}$. It is clear to see that $P_{ccw}$ has part of the squared-Lorentzian profile.

The SE will induce an intrinsic linewidth. In the above analysis (using the Lamb equation), we ignored the SE and obtained a steady-state solution, whose linewidth approaches zero, which is not true in a real lasing system (*50*). Here, we consider the temporal evolution for the number of photons for a lasing mode labeled $l$

$$\frac{d}{dt}N_l = \nu_0 N N_l + \nu_0 N_2 - 2(\gamma_0 + \gamma_1 + \gamma_2)N_l \quad (17)$$

In the steady state, we have $\frac{d}{dt}N_l = 0$; thus, the extra loss is $\delta_s = 2(\gamma_0 + \gamma_1 + \gamma_2) - \nu_0 N = \frac{\nu_0 N_2}{N_l}$. Here, $N_2$ represents the population of the upper lasing level. For the same pump power, the number $N_2$ for the control system and the ES system is nearly the same. However, as we show later, because of the higher energy efficiency for the ES system, the photon number of lasing mode for the ES system is higher than that of the control system, which leads to the compression of intrinsic linewidth for the ES system. Figure 2C numerically shows how the normalized linewidth at port 1 varies as the reflection-coefficient ratio of the left and right ports ($\kappa_l/\kappa_r$) increases. We observed how the linewidth changes as $\kappa_r$ decreases. The initial case corresponds to the control system with $\kappa_r = \kappa_l$. With the decreasing of $\kappa_r$, the linewidth rapidly decreases owing to the improvement of pump energy utilization between the two eigenmodes. The linewidth compressed to 37% in the ES-tailored system when $\kappa_r \ll \kappa_l$ compared with the control system. Figure 2D shows laser spectra when $\ln(\kappa_l/\kappa_r)$ is 0, 0.5, 1, 2, 5, and 10, respectively, which can clearly describe the change of the laser linewidth with the reflection-coefficient ratio. The ES-tailored unidirectional power flow in the microcavity could improve the utilization rate of pump energy, which includes the reduction of the lasing threshold and the improvement of the energy-conversion efficiency.

Here, we numerically calculated the photoluminescence (PL) intensity of the ES system below the lasing threshold. We set the PL intensity for the CW and CCW mode $I_{cw(ccw)}$, and we can write the dynamic evolution as follows

$$\frac{d}{dt}I_{cw} = -2(\gamma_0 + \gamma_1 + \gamma_2 - g_{PL})I_{cw} + \nu I_0 \quad (18)$$

$$\frac{d}{dt}I_{ccw} = -2(\gamma_0 + \gamma_1 + \gamma_2 - g_{PL})I_{ccw} + 2\gamma_1\kappa_l I_{cw} + \nu I_0 \quad (19)$$

where $I_0$ is the SE intensity and $g_{PL}$ is the gain rate for PL, which may not identical with the gain of the laser due to the incoherent property of PL. The steady-state solution is $I_{cw} = \frac{\nu I_0}{2(\gamma_0+\gamma_1+\gamma_2-g_{PL})}$ and $I_{ccw} = \frac{\nu I_0}{2(\gamma_0+\gamma_1+\gamma_2-g_{PL})} + \frac{2\gamma_1\kappa_l\nu I_0}{4(\gamma_0+\gamma_1+\gamma_2-g_{PL})^2}$. As the external pump power is increased, the ratio for $\frac{(I_{cw}+I_{ccw})_{ES}}{(I_{cw}+I_{ccw})_{CS}} = 1 + \frac{2\gamma_1\kappa_l}{\gamma_0+\gamma_1+\gamma_2-g_{PL}}$. Therefore, the PL intensity increases in the ES system compared to the control system. Thus, the lasing threshold may be decreased because of the increase in stimulated emission, as the stimulated emission spectrum is the same as the PL spectrum (*51*). Here, we point out that the gain rate can be affected by many other factors, which may also reduce the lasing threshold. For example, we chose $g_{PL} = 0$ to calculate the SE, which could also be increased and, hence, to increase the stimulated emission rate.

Moreover, the energy-conversion efficiency could also be improved in the ES-tailored system. In the control system, we have $|E_{cw}|^2 = |E_{ccw}|^2 = \left(1 - \frac{\gamma}{v_0 N}\right)\frac{1}{S+C}$, while in the ES case, we have $|E_{cw}|^2 = 0$, $|E_{ccw}|^2 = \left(1 - \frac{\gamma}{v_0 N}\right)\frac{1}{S}$. We considered the fact that the gain rate is proportional to the SE rate and inversion number $N$, where $N$ is proportional to the pump rate. The slope for the control system $\frac{\partial}{\partial N}(|E_{cw}|^2 + |E_{ccw}|^2)|_{g=\gamma} = \frac{2\gamma}{v(S+C)}$ and that for the ES system $\frac{\partial}{\partial N}(|E_{cw}|^2 + |E_{ccw}|^2)|_{g=\gamma} = \frac{\gamma}{vS}$. In the vicinity above the lasing threshold ($g = \gamma$), the slope efficiency for ES system is $\frac{(C+S)v_{CS}}{2Sv_{ES}}$ that of the control system. Hence, we found that the slope is increased in the ES system, resulting in a higher energy efficiency, which agrees with the experimental observation that the SE rate for the ES system is almost twice as the control system.

An imperfection such as a scatterer introduced in the fabrication process would affect the off-diagonal elements and cause intermodal coupling, which would lead to the mode splitting. Such a splitting can be used for sensing enhancement (*22*, *36*, *52*). In the Supplementary Materials, we gave a detailed discussion about the effect of the small perturbation in the off-diagonal term on lasing performance. We found that while the imperfection-induced intermodal coupling would indeed cause the mode splitting, such splitting can hardly influence our main lasing result.

We experimentally realized the above scheme using prepared $CsPbBr_3$ single-crystal thin films (SCTFs). The micro/nanostructures were fabricated on a 300-nm-thick $CsPbBr_3$ SCTF with ultrahigh uniformity and optical gain (*38*) that behaves as a lossy material in the absence of external pumping. The microcavity was vertically pumped by an external femtosecond pulsed laser, inducing optical gain in the microcavity. The MW remained in the lossy state to realize the asymmetrical reflection. Here, for demonstration, we adopted the configuration of a side-coupled straight waveguide below the microcavity. For the control system, a lower waveguide was placed symmetrically relative to the microcavity. We used the finite-element method (provided by the COMSOL Multiphysics commercial software) to conduct simulations of eigenmode distribution of the ES-tailored system in the absence of external pumping.

The top-right inset of Fig. 1C demonstrates the calculated cross-sectional electric-field distribution in the $CsPbBr_3$ waveguide with a width of 150 nm and a height of 300 nm, which shows that the designed waveguide confines the light field well. The MW was placed asymmetrically relative to the microcavity. The length asymmetry at the left and right sides of the MW relative to the microcavity aimed to make the reflection coefficient on the left side much larger than that on the right side, i.e., $\kappa_l \gg \kappa_r$. Figure 1C shows the simulated electric-field distribution of the eigenmode of the ES-tailored system, where the diameter of the microcavity is 3 μm. The red arrows on the field-distribution surface, representing the time-averaged power outflow of the light field in the microcavity, illustrate the excellent one-way mode propagation. Figure 1D shows a top-view scanning electron microscopy (SEM) image and a tilted SEM image at 52° (inset) of the fabricated $CsPbBr_3$ ES-tailored sample. The schematic diagram of the lasing experiment for this sample is shown in Fig. 3A.

### Second-order ES–tailored microlaser

To verify the lasing characteristics of the $CsPbBr_3$ control sample (shown in Fig. 3Bi), we obtained a PL image above the pump threshold (shown in Fig. 3Bii). The $CsPbBr_3$ microcavity had a diameter of 3 μm, and the light intensity of the left and right ports of the TW was essentially identical. Figure 3E shows the measured emission intensity (blue) and full width at half maximum (FWHM) (red) at the left port as a function of the pumping power excited by a 400-nm femtosecond pulsed laser. The spot diameter of the pumping light was focused to selectively cover the microcavity using a 100× objective lens. Moreover, the spatially resolved optical measurement system supports the selective collection of spectral signals of specific microregions through adjustment of the size and position of adjustable holes at the signal-collecting end. At the lasing threshold of 5.4 μJ/cm$^2$, the PL spectrum showed a sharply reduced FWHM and a greatly increased intensity simultaneously. When the pump fluence was further increased, the narrower linewidth and the superlinear increase in the intensity indicated the achievement of lasing action. Figure S13A shows the pump fluence–dependent emission spectrum for the control system. When the pumping density was low, there was only a single emission spectrum of a broad PL peak centered at 525 nm with an FWHM of ~17 nm owing to SE. When the pump fluence exceeded 5.4 μJ/cm$^2$, a sharp peak centered at 535 nm emerged with an FWHM of ~1.2 nm at the lower-energy tail.

Similarly, to study the lasing characteristics of the $CsPbBr_3$ ES-tailored sample (shown in Fig. 3Ci), we obtained a PL image with excitation above the pump threshold (shown in Fig. 3Cii). The light-intensity contrast between the left and right ports of the TW remained stable and reached as high as ~12 dB, indicating that the microcavity in the ES-tailored system achieved an almost-perfect unidirectional CCW mode. The pump fluence–dependent emission spectrum for the system is shown in fig. S13B. When the pump power was relatively low, a broad SE band centered at 526 nm with an FWHM of ~16.4 nm was obtained. At the threshold pump fluence (2.4 μJ/cm$^2$), a sharp peak with a compressed FWHM emerged. Figure 3F shows the pump fluence–dependent emission intensity (blue) and FWHM (red). When the pump fluence reached 2.4 μJ/cm$^2$, a sharp peak centered at 537 nm emerged with an FWHM of ~0.8 nm at the lower-energy tail. When comparing the lasing results for the ES-tailored sample with those for the control sample, the energy-conversion efficiency ($x$-intercept of the emission intensity curve) in the ES-tailored sample was 1.91 times higher than the control sample, and the pump threshold was reduced to 44%. It can also be seen from Fig. 3D that the laser linewidth was reduced to 67%. These observations demonstrate the superiority and feasibility of our ES-tailored strategy. Here, we can see that the laser spectrum in the ES system has a red shift of about 2.1 nm compared with the control system. We note that a larger excitation density corresponds to a decrease in the refractive index (*53*). In the ES system, lower lasing threshold leads to a lower carrier density, which would increase the index. Thus, the shift phenomenon originates from the lower density of carriers in the ES system.

The lasing linewidth observed in the experiment is affected by many factors. Some earlier studies attributed the lasing in $CsPbBr_3$ to the stimulated emission due to electron-hole coupling (*53*), while others attributed the lasing mechanism to excitons (*54*). Whatever the real essential mechanism is, the linewidth for $CsPbBr_3$

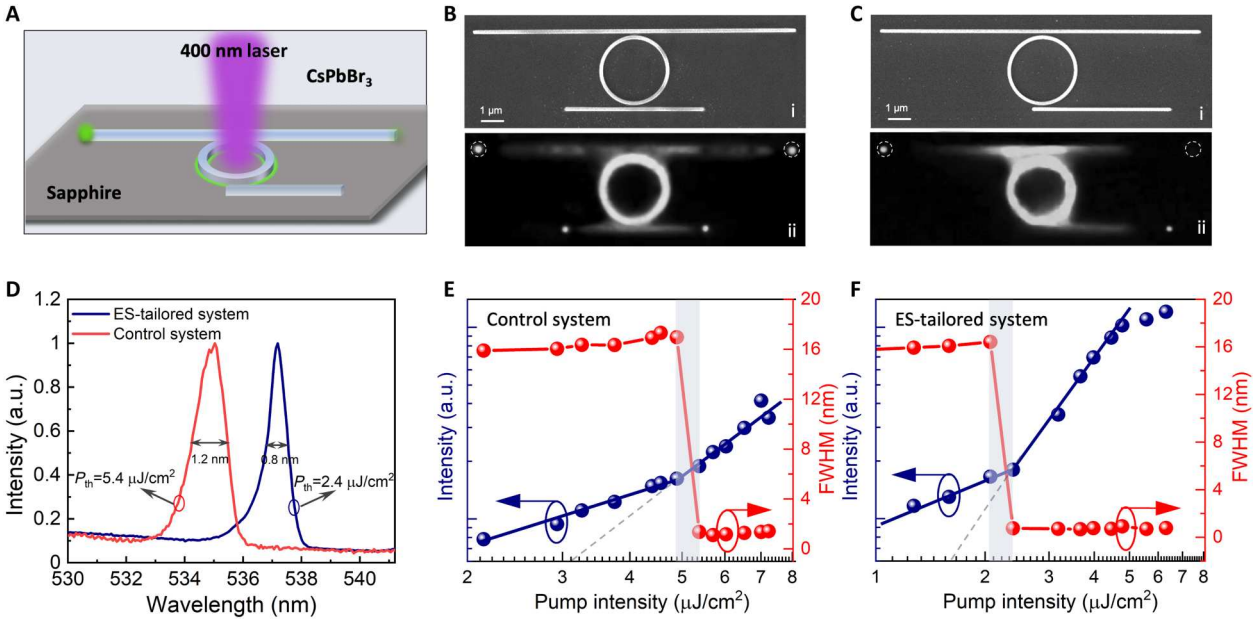


**Fig. 3. Lasing experiment on the exceptional surface (ES)–tailored microlaser.** (**A**) Schematic diagram of the experiment for the ES-tailored $CsPbBr_3$ microcavity-modulation waveguide (MW)-transmission waveguide (TW) coupled system. (**B**) (i) Top-view SEM image of the control system, with the lower MW placed symmetrically relative to the microcavity. Scale bar, 1 μm. (ii) Photoluminescence (PL) image of the control system, with 400-nm femtosecond laser excitation above the pump threshold. The essentially identical light intensity spots on the left and right ports of the TW are circled with a white dashed circle. (**C**) (i) Top-view SEM image of the ES-tailored system. Scale bar, 1 μm. (ii) PL image of the system, with excitation above the pump threshold. The stable and high light-intensity contrast between the left and right ports of the TW is shown by the white dashed circles, indicating that the microcavity in the ES-based system has reached an almost-perfect unidirectional counterclockwise (CCW) mode. (**D**) Comparison of the lasing results for the control system and the ES-tailored system. The laser linewidth is compressed to 67%, and the pump threshold is reduced to 44%, indicating the superiority and feasibility of our proposed strategy of microlaser. (**E**) Pump fluence-dependent PL intensity (blue) and full width at half maximum (FWHM) (red) for the control system, showing a threshold of 5.4 μJ/cm$^2$ and a lasing FWHM of 1.2 nm when the pump intensity increased from 2.1 to 7.2 μJ/cm$^2$. (**F**) Pump fluence-dependent emission intensity (blue) and FWHM (red) of the ES-tailored system when the pump intensity increased from 0.7 to 6.3 μJ/cm$^2$, demonstrating a compressed FWHM of approximately 0.8 nm at the threshold pump fluence of 2.4 μJ/cm$^2$. The energy-conversion efficiency (*x*-intercept of the emission intensity curve) in the ES-tailored sample is 1.91 times higher than the control sample.

lasing also depends on the density of carriers (*53*). Both of the theoretical discussion and the experimental observations above demonstrate that the lasing threshold for the ES system can be reduced, which will decrease the carrier density and contributes to the compression of lasing linewidth.

To gain further insight into the performance of the ES-tailored system, we gradually increase the length of the right side of the MW, i.e., gradually reduce $\kappa_r$, and observed changes in the contrast of the light intensity at both end ports of the TW. The corresponding process in theory is to make the system gradually approached and then remained in the ES condition. Figure 4A depicts PL images above the lasing threshold of microlasers with MW lengths ranging from 0 to 10 μm. In this figure, the gray arrow indicates the length-change direction of the MW. The area surrounded by the red (blue) circle represents the light intensity at the left (right) end port of the TW. The PL images illustrate that when the right side of the MW gets longer, the intensity contrast between the two ports of the TW increases. Figure 4B shows how the right length of MW affects both the intensity contrast of the left and right ports of the TW and the linewidth of the left port. When the MW length reaches 6 μm, the contrast tends to saturate at approximately 12 dB, which indicates that the unidirectional mode in the microcavity is well realized, and the system reaches a stable ES. As the right length of MW increases, the linewidth initially rises and then falls rapidly, which is consistent with theoretical analysis.

Because of the gain saturation effect, the gain for other modes increases and reaches their threshold to lase as the pump power is further increased. The laser mode of the microcavity then evolves from single mode to multimode. The performance of the strategy does not depend on the specific resonant mode in the microcavity; i.e., different laser modes satisfy the unidirectional lasing emission scheme for the proposed ES-tailored system. Figure 4C shows how the pump power affects the measured laser spectrums of the left (solid lines) and right (dotted lines) ports of the TW. As the pump power increases from 7.0 to 12.6 μJ/cm$^2$, the laser mode changes from single mode to dual mode and then to triple mode. Each laser mode at the left port 1 has the characteristics of linewidth compression compared with the laser modes at the right port 2. Moreover, high-contrast one-way emission is realized between the two ports of the TW with an average contrast of approximately 10.2 dB. It should be noted that, here, we mainly focused on the scheme itself, and we did not optimize the size of the microcavity to reach a lower intrinsic loss or experimentally optimize the micro/nanofabrication process on the perovskite material system. Apparently, this scheme can be used in an optimized laser system to further improve the lasing performance.

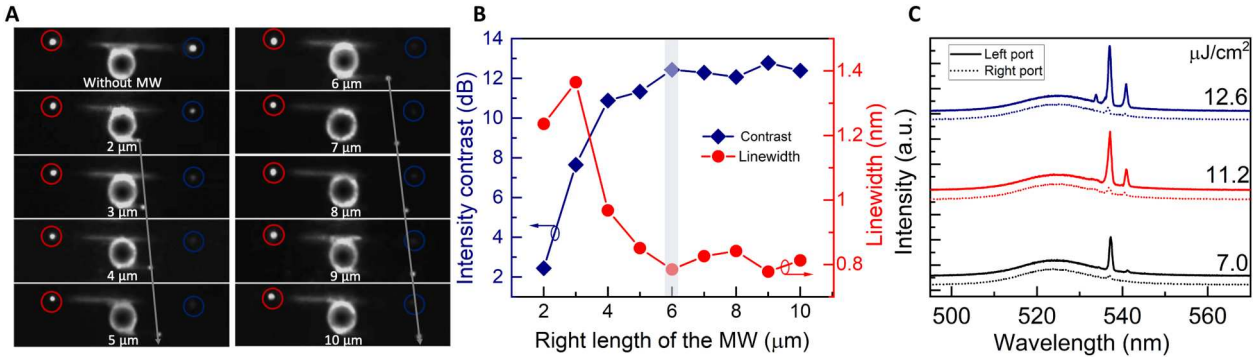


**Fig. 4. Further performance of the exceptional surface (ES)–tailored microlaser.** (**A**) Photoluminescence (PL) images above the lasing threshold of microcavity-modulation waveguide (MW)-transmission waveguide (TW) coupled systems with MW lengths ranging from 0 to 10 μm. The gray arrow indicates the direction of change of the MW. The area surrounded by the red (blue) circle represents the light intensity at the left (right) end of the TW. The contrast between the two sides of the TW increases as the right side of the MW gets longer. (**B**) Impact of the right length of MW on the intensity contrast of the left and right ports of the TW (blue) and the linewidth of the left port of the TW (red). The contrast tends to saturate at approximately 12 dB when the right length of MW reaches 6 μm, indicating that the system reaches a stable ES. As the right length of MW increases, the linewidth initially rises and then falls rapidly, which is consistent with theoretical analysis. (**C**) Laser spectrum of the left port 1 (solid curves) and right port 2 (dotted curves) of the TW as the pump power is increased from 7.0 to 12.6 μJ/cm$^2$. The laser modes change from single mode to dual mode and then to triple mode. The high-contrast one-way emission with an average contrast of approximately 10.2 dB and the linewidth compression result are applicable to different laser modes.

## Scalability of the proposed strategy

Non-Hermitian coupled resonator arrays have been realized and studied with different construction schemes (*17*, *18*, *55*). Here, the proposed ES-tailored microlaser strategy can be easily extended from second-order to higher-order cases, which is more robust compared with other schemes (*22*, *56*). Here, we use a common TW to provide unidirectional couplings among modes of microcavities tailored by second-order ESs. Thus, second-order ESs are merged into a higher-order ES (Fig. 5A). As an example, we take the realization of a fourth-order ES. Suppose the system contains two second-order ES–tailored microcavities modulated by a side-coupled unclosed ring and a common TW to provide unidirectional coupling of the two microcavities. The study method is similar to that of the second-order ES–tailored system. The Hamiltonian of the fourth-order system obtained from TCMT can be written as

$$H = \begin{bmatrix} \omega_0 - \omega - i\alpha & 0 & 0 & 0 \\ -2\gamma_1\kappa_l e^{i\phi_l} & \omega_0 - \omega - i\alpha & 0 & -2\gamma_2\kappa_w e^{i\phi_w} \\ -2\gamma_2\kappa_w e^{i\phi_w} & 0 & \omega_0 - \omega - i\alpha & 0 \\ 0 & 0 & -2\gamma_1\kappa_l e^{i\phi_l} & \omega_0 - \omega - i\alpha \end{bmatrix} \tag{20}$$

Here,$\alpha = \gamma_0 + \gamma_1 + \gamma_2 - g$, $\kappa_w$ is the propagating-efficiency coefficient, $\phi_w$ is the propagation phase in TW between the nearest-neighbor microcavity, and the other parameters of the system are consistent with those of the second-order case. The four rows of the matrix, from top to bottom, represent the CW and CCW mode of the left microcavity (labeled 1) and the CW and CCW mode of the right microcavity (labeled 2), respectively. We can also write down the Lamb equation of this system just as we did before. The eigenvalues and eigenstates of four-order Hamiltonian is $\omega_0 - i\alpha$ and $[0\ 1\ 0\ 0]^T$ with fourfold degenerate. The same is true when realizing higher-order ESs. We also analyzed the PL spectrum intensity as we did in second-order ES part. Here, we simply set $g_{PL} = v$; i.e., the gain rate for PL is proportional to extra pump power without considering the internal complex mechanism. Under this assumption, $I_{n,\mathrm{tot}} = \frac{vI_0}{2(\gamma_0+\gamma_1+\gamma_2-v)} + \frac{n\gamma_1 vI_0}{2(\gamma_0+\gamma_1+\gamma_2-v)^2}$, which indicates that the total PL intensity increases linearly with the order of the ES. Here, we use the same method to analyze the lasing performance. The lasing threshold condition is $I_{n,\mathrm{tot}} = I_{\mathrm{th}}$; thus, the threshold $v_{\mathrm{th}}$ decreases with the increase of $n$. Similarly, the energy-conversion efficiency could also be further improved and the linewidth would be compressed with the increase of $n$. Figure 5B shows the real and imaginary parts of the eigenvalues as a function of the reflection-coefficient ratio of the MW ($\kappa_l/\kappa_r$) and the associated parameter $\delta$ for systems of different orders of ESs, which illustrates the process of the gradual degeneration of the eigenvalues (hypersurface of EPs for different orders). Figure 5C shows the normalized intrinsic lasing linewidth and energy-conversion efficiency as a function of the order of the ES. An even narrower linewidth can be realized by constructing higher-order ES–tailored systems, and the improvement of energy-conversion efficiency is proportional to $n$.

Our scalable ES-tailored microlaser strategy has many potential effects and applications. Here, we consider a topological microlaser based on the Su-Schrieffer-Heeger (SSH) model as an example to illustrate the contribution of our strategy to the joint research direction of non-Hermitian photonics and topological photonics. We consider lining up several microcavities originally tailored by second-order ESs and setting them to be close to each other and coupled to their two nearest neighbors. The distance between the microcavities alternates between being long and short so that the two coupling coefficients are different. Given the non-Hermitian modulation of second-order ESs in each microcavity, the Hamiltonian for the SSH model can be modified as

$$H_{ij} = \begin{cases} \omega_0 - \omega - i\alpha, & i = j \\ -2i\gamma_1\kappa_l e^{i\phi_l}, & i = 2n;\ j = 2n-1 \\ 2\gamma_n, & (i,j) = (4m+1, 4m-1); (i,j) = (4m+1, 4m) \\ 2\gamma_f, & (i,j) = (4n, 4n-3); (i,j) = (4n-1, 4n-2) \end{cases} \tag{21}$$

where $i, j = 1,2, \ldots, 4N$, $N$ is the number of microcavities, $n = 1,2, \ldots, N$, $m = 1,2, \ldots, N-1$, and $\gamma_n/\gamma_f$ is the coupling-coefficient ratio for

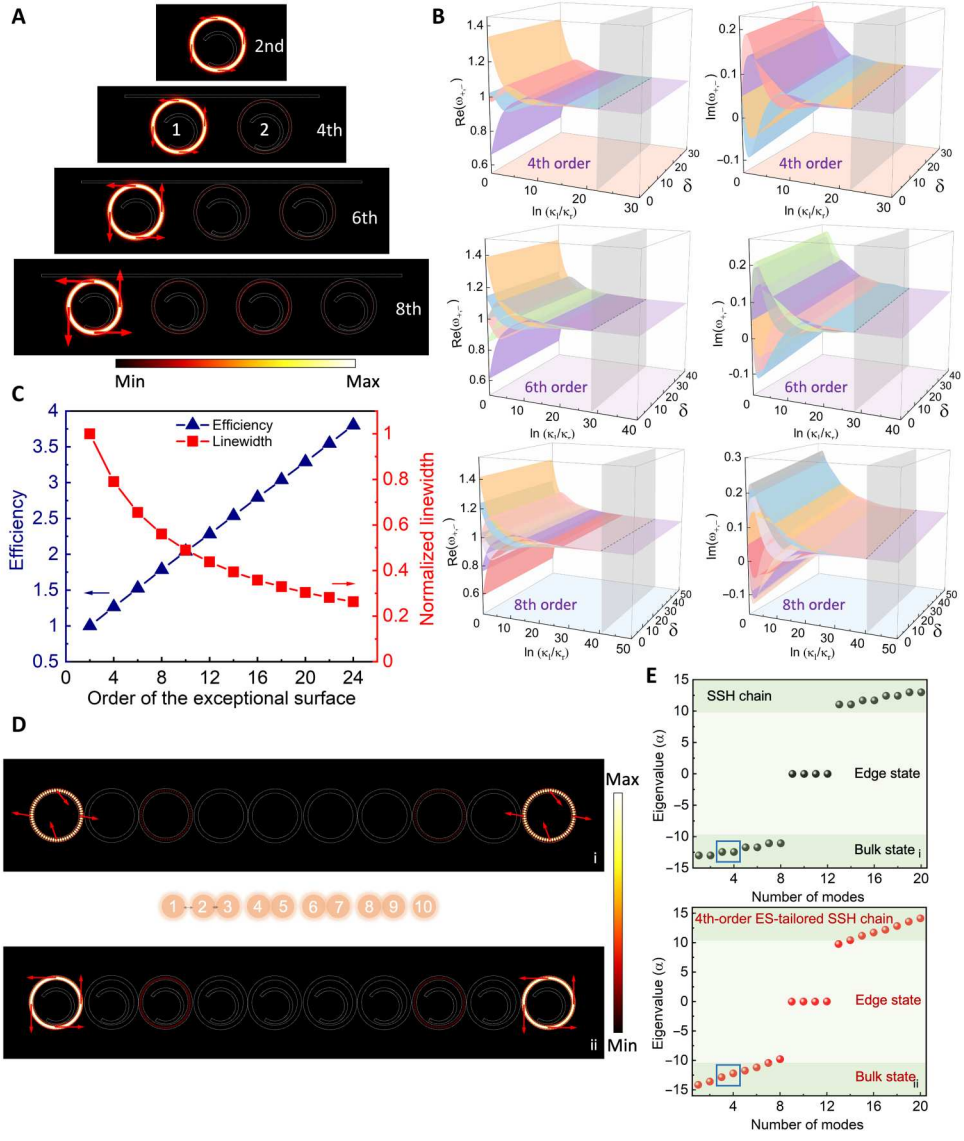


**Fig. 5. Scalability of the proposed exceptional surface (ES)–tailored microlaser strategy.** (**A**) Simulation results for the field distributions of higher-order ESs using a common transmission waveguide (TW) to provide unidirectional couplings among modes of second-order ES-tailored microcavities. (**B**) Real and imaginary parts of the eigenvalues of the system varying with the reflection-coefficient ratio of the modulation waveguide (MW) ($\kappa_l/\kappa_r$) and the associated parameter $\delta$ for systems of different orders of ESs, which illustrates the process of the gradual degeneration of the eigenvalues [hypersurface of exceptional points (EPs) for different orders]. (**C**) Lasing efficiency (blue) and the linewidth (red) at the left port of the TW versus the order of the ES. An even narrower linewidth and higher energy-conversion efficiency can be realized by constructing higher-order ESs. (**D**) Simulation results for the field distributions of (i) the microcavity Su-Schrieffer-Heeger (SSH) chain without non-Hermitian ES modulation (the four edge modes on both sides of the chain behave as standing waves), for comparison, and (ii) the microcavity SSH chain with non-Hermitian ES modulation [the four edge modes eventually evolve into degenerate counterclockwise (CCW) traveling-wave modes]. (**E**) Energy-eigenvalue distribution varying with the number of eigenmodes in the system for (i) the microcavity SSH chain without non-Hermitian ES modulation, for comparison, and (ii) the fourth-order ES-tailored microcavity SSH chain. The blue boxed areas in the two distributions show that the non-Hermitian modulation breaks a certain degree of symmetry of the status of the two surrounding orientation modes in the system, i.e., clockwise (CW) and CCW modes in each microcavity.

the cases of a nearer/farther distance between the two nearest microcavities. The calculated eigenvalues and eigenmodes of the system indicate that the SSH chain with non-Hermitian modulation is on the fourth-order ES.

As shown in Fig. 5D, we simulated field distributions of eigenmodes (20 modes) in a system containing 10 microcavities. A configuration of 10 microcavities without non-Hermitian modulation was used as a control system. The field distributions show that for the microcavity SSH chain without modulation, the four edge modes on both sides of the chain behave as standing waves. By contrast, for the chain with modulation, the four edge modes eventually evolve into degenerate CCW traveling-wave modes. Figure 5E shows that the energy-eigenvalue distributions vary with the number of eigenmodes. Both SSH chains have four degenerate eigenvalues in the bandgap. Simultaneous degeneration of these four eigenvalues and the corresponding four eigenmodes means that the chain with non-Hermitian modulation is on the fourth-order ES. The energy-eigenvalue distribution of the fourth-order ES-tailored

microcavity SSH chain is not as symmetrical as that of the control system shown in the blue boxed area, because the non-Hermitian modulation breaks a certain degree of symmetry of the status of the two surrounding orientation modes in the system, i.e., CW and CCW modes in each microcavity. When the number of non-Hermitian–modulated microcavities is odd, there is a second-order degeneration of both eigenvalues and eigenmodes, as shown in fig. S11. The energy-conversion efficiency is four times larger compared with that of the control system. Therefore, a micro/nanolaser based on a topological laser scheme with modulation of a non-Hermitian ES can be provided with both dual robustness (topological and ES) and excellent performance. This performance includes linewidth compression and improvement in energy-conversion efficiency, which further proves the potential application of our proposed strategy.

The large-area micro/nanofabrication technology with high luminescence quantum efficiency and good repeatability for this material of single-crystal $CsPbBr_3$ thin film is not yet mature, and it is still a challenge to selectively pump the microcavity while keeping the modulated waveguide in an unpumped lossy state even with the utilization of the spatial light modulator because the damage threshold of the spatial light modulator to femtosecond pulsed light and the stability of the measurement need to be considered comprehensively. Therefore, further developing the micro/nanofabrication technology for perovskite materials and improving the experimental test system will enable high-order ES systems and ES-tailored topological microlasers to be well demonstrated in the near future.

## DISCUSSION

We proposed a strategy of robust on-chip visible-light microlaser based on the ES. We then experimentally verified the feasibility of this strategy using a $CsPbBr_3$ laser system benefiting from physical design and excellent material properties. The ES-tailored system compresses the laser linewidth effectively and notably reduces the pump threshold and improves the energy-conversion efficiency. An even narrower linewidth with a higher peak intensity and a higher pump energy utilization efficiency can be easily realized by constructing higher-order ESs. Discussion of an ES-tailored topological microlaser with a unique performance proved the potential impact and applications of our strategy. This work provides a feasible solution for the implementation of integrated high-speed visible-light communication and on-chip ultralow-energy-consumption information-processing chips, with the TW replaced with low-loss materials compatible with CMOS (complementary metal-oxide-semiconductor) technology. In addition, the work opens research directions for non-Hermitian photonics with nonlinear optics and topological photonics.

## MATERIALS AND METHODS

### Preparation of $CsPbBr_3$ SCTFs and structure characterization

Chemical vapor deposition methods were used to prepare $CsPbBr_3$ SCTFs in a Thermo Fisher Scientific single-zone tube-furnace system. Halides and lead salts were purchased from Sigma-Aldrich and included CsBr (99.999%) and $PbBr_2$ (99.999%). A *c*-plane double-sided polished sapphire was purchased from Nanjing MKNANO Tech. Co. Ltd. CsBr (5 mg) and $PbBr_2$ (7 mg) were mixed thoroughly before being placed at the center of the heating zone of the tube furnace. After the substrates were placed inside the tube furnace, the quartz tube was pumped down and cleaned with high-purity Ar (99.999%) for 20 min. Then, a 60-sccm (standard cubic centimeters per minute) flow of high-purity Ar was introduced into the tube, and the pressure was maintained at 600 torr. The furnace was moved to the reaction area once it reached the setting temperature of 600°C from room temperature. This temperature was maintained for 10 min, and then, the furnace was cooled to room temperature naturally. SEM imaging was performed with a beam voltage of 10 kV using an ultrahigh-resolution cold field-emission scanning electron microscope (Hitachi-SU8220). Selected-area electron diffraction analysis was conducted using a field-emission transmission electron microscope (Tecnai G2 F20 U-TWIN), and x-ray diffraction (Rigaku D/max-TTRIII, Cu Kα radiation) was performed to confirm the phase of the prepared films.

### Optical characterization of the $CsPbBr_3$ SCTFs

#### *PL spectra*

To obtain the PL spectra, the emission from a 405-nm CW laser was focused to a spot size of 2 μm through a 100× objective lens. The PL emission signal was collected by the same microscope objective into an optical fiber and analyzed by a Princeton Instrument SP2500i spectrometer equipped with a liquid nitrogen–cooled charge-coupled device (CCD). The PL image was recorded by a CCD equipped on an Olympus BX51 microscope. A 442-nm long-pass filter was used to block the pump laser.

#### *Time-resolved PL measurements*

The central wavelength of a Coherent Mira 900 laser (central wavelength: 800 nm, pulse length: 120 fs, repetition rate: 76 MHz) was frequency doubled by a barium metaborate (BBO) crystal to produce a 400-nm pulsed laser as the excitation source. The PL lifetime was obtained by a time-corrected single-photon counter (SPC-150), which had an ultimate temporal resolution of ~40 ps.

#### *Transient absorption measurements*

The 400-nm pump laser was obtained by frequency doubling (800 nm, 100 fs, 1 kHz) with a BBO crystal. The power-dependent transient absorption (TA) spectra of the perovskite SCTFs were realized using an Ultrafast System HELIOS TA spectrometer. $CsPbBr_3$ SCTFs grown on sapphire substrates were tested directly.

#### *ASE and optical-gain measurements*

The pump source in the amplified spontaneous emission (ASE) measurement was identical to that used for the lasing test. In the variable-stripe-length experiments, the laser beam was focused to form a uniform strip light (width: 200 μm, length: 1 cm) by a cylindrical lens. A vernier caliper was used to control the length of the strip light while keeping the width of the spot unchanged. In the ASE measurement, the length of the strip light was fixed, while the pump power was varied; for the gain testing, the reverse condition was applied.

### Fabrication of the microlaser

Devices were fabricated by leveraging the microfabrication technology of focused-ion-beam etching. The structures on a chip were etched in 300-nm-thick $CsPbBr_3$ SCTFs on the sapphire substrate using an SEM and a focused-ion-beam DualBeam system (FEI Helios NanoLab 600i). To achieve higher etching precision and minimize the surface damage caused by the ion beam, a smaller

ion-beam current was used for etching. Here, the beam current was 7.7 pA, and the beam voltage was 30 kV.

### Lasing characterization of the microlaser

An Olympus BX51 optical microscope was used to obtain the lasing spectra. A 400-nm pulsed laser was used as the excitation source, which was frequency doubled by a BBO crystal from an amplifier laser source (Astrella, Coherent, central wavelength: 800 nm, repetition rate: 1 kHz, pulse width: 100 fs). To realize the selective excitation of an area, the spot diameter was focused to exactly cover the microcavity using a 100× objective lens. The emission signal was collected by the same objective and analyzed by a Princeton Instrument SP2500i spectrometer equipped with a liquid nitrogen–cooled CCD (PyLon CCD, Princeton Instruments).

## Supplementary Materials

**This PDF file includes:**

Supplementary Text
Table S1
Figs. S1 to S15
References

## REFERENCES AND NOTES


1. L. Grobe, A. Paraskevopoulos, J. Hilt, D. Schulz, F. Lassak, F. Hartlieb, C. Kottke, V. Jungnickel, K. D. Langer, High-speed visible light communication systems. *IEEE Commun. Mag.* **51**, 60–66 (2013).
2. P. H. Pathak, X. Feng, P. Hu, P. Mohapatra, Visible light communication, networking, and sensing: A survey, potential and challenges. *IEEE Commun. Surv. Tutor.* **17**, 2047–2077 (2015).
3. S. Wu, H. Wang, C. H. Youn, Visible light communications for 5G wireless networking systems: From fixed to mobile communications. *IEEE Netw.* **28**, 41–45 (2014).
4. R. Ji, S. Wang, Q. Liu, W. Lu, High-speed visible light communications: Enabling technologies and state of the art. *Appl. Sci.-Basel* **8**, 589 (2018).
5. C.-T. Tsai, C.-H. Cheng, H.-C. Kuo, G.-R. Lin, Toward high-speed visible laser lighting based optical wireless communications. *Prog. Quantum Electron.* **67**, 100225 (2019).
6. K. Shafique, B. A. Khawaja, F. Sabir, S. Qazi, M. Mustaqim, Internet of Things (IoT) for next-generation smart systems: A review of current challenges, future trends and prospects for emerging 5G-IoT scenarios. *IEEE Access* **8**, 23022–23040 (2020).
7. Z. Ullah, F. Al-Turjman, L. Mostarda, R. Gagliardi, Applications of artificial intelligence and machine learning in smart cities. *Comput. Commun.* **154**, 313–323 (2020).
8. Z. Zhang, Y. Xiao, Z. Ma, M. Xiao, Z. Ding, X. Lei, G. K. Karagiannidis, P. Fan, 6G wireless networks vision, requirements, architecture, and key technologies. *IEEE Veh. Technol. Mag.* **14**, 28–41 (2019).
9. X. You, C. Wang, J. Huang, X. Gao, Z. Zhang, M. Wang, Y. Huang, C. Zhang, Y. Jiang, J. Wang, M. Zhu, B. Sheng, D. Wang, Z. Pan, P. Zhu, Y. Yang, Z. Liu, P. Zhang, X. Tao, S. Li, Z. Chen, X. Ma, C.-L. I, S. Han, K. Li, C. Pan, Z. Zheng, L. Hanzo, X. Shen, Y. J. Guo, Z. Ding, H. Haas, W. Tong, P. Zhu, G. Yang, J. Wang, E. G. Larsson, H. Q. Ngo, W. Hong, H. Wang, D. Hou, J. Chen, Z. Chen, Z.-C. Hao, G. Li, R. Tafazolli, Y. Gao, H. V. Poor, G. P. Fettweis, Y. C. Liang, Towards 6G wireless communication networks: Vision, enabling technologies, and new paradigm shifts. *Sci. China Inf. Sci.* **64**, 110301 (2021).
10. Y. C. Chi, D. H. Hsieh, C. T. Tsai, H. Y. Chen, H. C. Kuo, G. R. Lin, 450-nm GaN laser diode enables high-speed visible light communication with 9-Gbps QAM-OFDM. *Opt. Express* **23**, 13051–13059 (2015).
11. R. X. G. Ferreira, E. Xie, J. J. D. McKendry, S. Rajbhandari, H. Chun, G. Faulkner, S. Watson, A. E. Kelly, E. Gu, R. V. Penty, I. H. White, D. C. O'Brien, M. D. Dawson, High bandwidth GaN-based micro-LEDs for multi-Gb/s visible light communications. *IEEE Photonics Technol. Lett.* **28**, 2023–2026 (2016).
12. E. J. Bergholtz, J. C. Budich, F. K. Kunst, Exceptional topology of non-Hermitian systems. *Rev. Mod. Phys.* **93**, 015005 (2021).
13. R. El-Ganainy, K. G. Makris, M. Khajavikhan, Z. H. Musslimani, S. Rotter, D. N. Christodoulides, Non-Hermitian physics and PT symmetry. *Nat. Phys.* **14**, 11–19 (2018).
14. M. A. Miri, A. Alù, Exceptional points in optics and photonics. *Science* **363**, eaar7709 (2019).
15. L. Feng, Z. J. Wong, R. M. Ma, Y. Wang, X. Zhang, Single-mode laser by parity-time symmetry breaking. *Science* **346**, 972–975 (2014).
16. H. Hodaei, M. A. Miri, M. Heinrich, D. N. Christodoulides, M. Khajavikhan, Parity-time–symmetric microring lasers. *Science* **346**, 975–978 (2014).
17. H. Zhao, X. Qiao, T. Wu, B. Midya, S. Longhi, L. Feng, Non-Hermitian topological light steering. *Science* **365**, 1163–1166 (2019).
18. H. Zhao, P. Miao, M. H. Teimourpour, S. Malzard, R. El-Ganainy, H. Schomerus, L. Feng, Topological hybrid silicon microlasers. *Nat. Commun.* **9**, 981 (2018).
19. M. H. Teimourpour, M. Khajavikhan, D. N. Christodoulides, R. El-Ganainy, Robustness and mode selectivity in parity-time (PT) symmetric lasers. *Sci. Rep.* **7**, 10756 (2017).
20. W. Chen, Ş. K. Özdemir, G. Zhao, J. Wiersig, L. Yang, Exceptional points enhance sensing in an optical microcavity. *Nature* **548**, 192–196 (2017).
21. B. Peng, Ş. K. Özdemir, M. Liertzer, W. Chen, J. Kramer, H. Yılmaz, J. Wiersig, S. Rotter, L. Yang, Chiral modes and directional lasing at exceptional points. *Proc. Natl. Acad. Sci. U.S.A.* **113**, 6845–6850 (2016).
22. H. Hodaei, A. U. Hassan, S. Wittek, H. Garcia-Gracia, R. El-Ganainy, D. N. Christodoulides, M. Khajavikhan, Enhanced sensitivity at higher-order exceptional points. *Nature* **548**, 187–191 (2017).
23. M. Brandstetter, M. Liertzer, C. Deutsch, P. Klang, J. Schöberl, H. E. Türeci, G. Strasser, K. Unterrainer, S. Rotter, Reversing the pump dependence of a laser at an exceptional point. *Nat. Commun.* **5**, 4034 (2014).
24. Z. Zhang, P. Miao, J. Sun, S. Longhi, N. M. Litchinitser, L. Feng, Elimination of spatial hole burning in microlasers for stability and efficiency enhancement. *ACS Photonics* **5**, 3016–3022 (2018).
25. C. T. Pike, Spatial hole burning in CW dye lasers. *Opt. Commun.* **10**, 14–17 (1974).
26. R. Schatz, Longitudinal spatial instability in symmetric semiconductor lasers due to spatial hole burning. *IEEE J. Quantum Electron.* **28**, 1443–1449 (1992).
27. S. I. Azzam, A. V. Kildishev, R. M. Ma, C. Z. Ning, R. Oulton, V. M. Shalaev, M. I. Stockman, J. L. Xu, X. Zhang, Ten years of spasers and plasmonic nanolasers. *Light Sci. Appl.* **9**, 90 (2020).
28. E. I. Galanzha, R. Weingold, D. A. Nedosekin, M. Sarimollaoglu, J. Nolan, W. Harrington, A. S. Kuchyanov, R. G. Parkhomenko, F. Watanabe, Z. Nima, A. S. Biris, A. I. Plekhanov, M. I. Stockman, V. P. Zharov, Spaser as a biological probe. *Nat. Commun.* **8**, 15528 (2017).
29. Y. J. Lu, C. Y. Wang, J. Kim, H. Y. Chen, M. Y. Lu, Y. C. Chen, W. H. Chang, L. J. Chen, M. I. Stockman, C. K. Shih, S. Gwo, All-color plasmonic nanolasers with ultralow thresholds: Autotuning mechanism for single-mode lasing. *Nano Lett.* **14**, 4381–4388 (2014).
30. S. T. Ha, Y. H. Fu, N. K. Emani, Z. Pan, R. M. Bakker, R. Paniagua-Domínguez, A. I. Kuznetsov, Directional lasing in resonant semiconductor nanoantenna arrays. *Nat. Nanotechnol.* **13**, 1042–1047 (2018).
31. Y. Yu, A. Sakanas, A. R. Zali, E. Semenova, K. Yvind, J. Mørk, Ultra-coherent Fano laser based on a bound state in the continuum. *Nat. Photonics* **15**, 758–764 (2021).
32. Z. Q. Yang, Z. K. Shao, H. Z. Chen, X. R. Mao, R. M. Ma, Spin-momentum-locked edge mode for topological vortex lasing. *Phys. Rev. Lett.* **125**, 013903 (2020).
33. D. Korn, M. Lauermann, S. Koeber, P. Appel, L. Alloatti, R. Palmer, P. Dumon, W. Freude, J. Leuthold, C. Koos, Lasing in silicon-organic hybrid waveguides. *Nat. Commun.* **7**, 10864 (2016).
34. J. Wiersig, S. W. Kim, M. Hentschel, Asymmetric scattering and nonorthogonal mode patterns in optical microspirals. *Phys. Rev. A* **78**, 053809 (2008).
35. J. Wiersig, A. Eberspächer, J. B. Shim, J. W. Ryu, S. Shinohara, M. Hentschel, H. Schomerus, Nonorthogonal pairs of copropagating optical modes in deformed microdisk cavities. *Phys. Rev. A* **84**, 023845 (2011).
36. Q. Zhong, J. Ren, M. Khajavikhan, D. N. Christodoulides, Ş. K. Özdemir, R. El-Ganainy, Sensing with exceptional surfaces in order to combine sensitivity with robustness. *Phys. Rev. Lett.* **122**, 153902 (2019).
37. Q. Zhong, S. K. Ozdemir, A. Eisfeld, A. Metelmann, R. El-Ganainy, Exceptional-point-based optical amplifiers. *Phys. Rev. Appl.* **13**, 014070 (2020).
38. Y. Zhong, K. Liao, W. Du, J. Zhu, Q. Shang, F. Zhou, X. Wu, X. Sui, J. Shi, S. Yue, Q. Wang, Y. Zhang, Q. Zhang, X. Hu, X. Liu, Large-scale thin $CsPbBr_3$ single-crystal film grown on sapphire via chemical vapor deposition: Toward laser array application. *ACS Nano* **14**, 15605–15615 (2020).
39. G. Liu, S. Jia, J. Wang, Y. Li, H. Yang, S. Wang, Q. Gong, Toward microlasers with artificial structure based on single-crystal ultrathin perovskite films. *Nano Lett.* **21**, 8650–8656 (2021).
40. W. Suh, Z. Wang, S. Fan, Temporal coupled-mode theory and the presence of non-orthogonal modes in lossless multimode cavities. *IEEE J. Quantum Electron.* **40**, 1511–1518 (2004).
41. R. R. Chasman, P. Ring, Diabolic points in deformation space. *Phys. Lett. B* **237**, 313–316 (1990).

42. A. P. Seyranian, O. N. Kirillov, A. A. Mailybaev, Coupling of eigenvalues of complex matrices at diabolic and exceptional points. *J. Phys. A Math. Gen.* **38**, 1723–1740 (2005).
43. S. Soleymani, Q. Zhong, M. Mokim, S. Rotter, R. El-Ganainy, Ş. K. Özdemir, Chiral and degenerate perfect absorption on exceptional surfaces. *Nat. Commun.* **13**, 599 (2022).
44. W. E. Lamb Jr., Theory of an optical maser. *Phys. Rev.* **134**, A1429–A1450 (1964).
45. L. N. Menegozzi, W. E. Lamb Jr., Theory of a ring laser. *Phys. Rev. A* **8**, 2103–2125 (1973).
46. M. Sorel, P. J. R. Laybourn, A. Scirè, S. Balle, G. Giuliani, R. Miglierina, S. Donati, Alternate oscillations in semiconductor ring lasers. *Opt. Lett.* **27**, 1992–1994 (2002).
47. K. Takata, K. Nozaki, E. Kuramochi, S. Matsuo, K. Takeda, T. Fujii, S. Kita, A. Shinya, M. Notomi, Observing exceptional point degeneracy of radiation with electrically pumped photonic crystal coupled-nanocavity lasers. *Optica* **8**, 184–192 (2021).
48. Q. Zhong, S. Nelson, Ş. K. Özdemir, R. El-Ganainy, Controlling directional absorption with chiral exceptional surfaces. *Opt. Lett.* **44**, 5242–5245 (2019).
49. Q. Zhong, A. Hashemi, Ş. K. Özdemir, R. El-Ganainy, Control of spontaneous emission dynamics in microcavities with chiral exceptional surfaces. *Phys. Rev. Res.* **3**, 013220 (2021).
50. A. L. Schawlow, C. H. Townes, Infrared and optical masers. *Phys. Rev.* **112**, 1940–1949 (1958).
51. A. Dogariu, A. J. Heeger, H. Wang, Photophysics of poly(2, 3-diphenyl-5-hexyl-*p*-phenylene vinylene). *Phys. Rev. B* **61**, 16183–16186 (2000).
52. G. Q. Qin, R. R. Xie, H. Zhang, Y. Q. Hu, M. Wang, G. Q. Li, H. Xu, F. Lei, D. Ruan, G. L. Long, Experimental realization of sensitivity enhancement and suppression with exceptional surfaces. *Laser Photonics Rev.* **15**, 2000569 (2021).
53. A. P. Schlaus, M. S. Spencer, K. Miyata, F. Liu, X. Wang, I. Datta, M. Lipson, A. Pan, X. Y. Zhu, How lasing happens in $CsPbBr_3$ perovskite nanowires. *Nat. Commun.* **10**, 265 (2019).
54. W. Du, S. Zhang, Z. Wu, Q. Shang, Y. Mi, J. Chen, C. Qin, X. Qiu, Q. Zhang, X. Liu, Unveiling lasing mechanism in $CsPbBr_3$ microsphere cavities. *Nanoscale* **11**, 3145–3153 (2019).
55. H. Schomerus, J. Wiersig, Non-Hermitian-transport effects in coupled-resonator optical waveguides. *Phys. Rev. A* **90**, 053819 (2014).
56. Q. Zhong, J. Kou, Ş. K. Özdemir, R. El-Ganainy, Hierarchical construction of higher-order exceptional points. *Phys. Rev. Lett.* **125**, 203602 (2020).
57. L. Zhao, Y. Gao, M. Su, Q. Shang, Z. Liu, Q. Li, Q. Wei, M. Li, L. Fu, Y. Zhong, J. Shi, J. Chen, Y. Zhao, X. Qiu, X. Liu, N. Tang, G. Xing, X. Wang, B. Shen, Q. Zhang, Vapor-phase incommensurate heteroepitaxy of oriented single-crystal $CsPbBr_3$ on GaN: Toward integrated optoelectronic applications. *ACS Nano* **13** (9), 10085–10094 (2019).
58. Y. Gao, L. Zhao, Q. Shang, Y. Zhong, Z. Liu, J. Chen, Z. Zhang, J. Shi, W. Du, Y. Zhang, S. Chen, P. Gao, X. Liu, X. Wang, Q. Zhang, Ultrathin $CsPbX_3$ nanowire arrays with strong emission anisotropy. *Adv. Mater.* **30**, 1801805 (2018).



**Acknowledgments**

**Funding:** This work was supported by the National Key Research and Development Program of China under grant no. 2018YFB2200403; the National Natural Science Foundation of China under grant nos. 91950204, 92150302, 22073022, and 11874130; the Ministry of Science and Technology under grant no. 2017YFA0205004; the Strategic Priority Research Program of Chinese Academy of Sciences under grant no. XDB36000000; and the DNL Cooperation Fund, CAS under grant no. DNL202016. Work done in Hong Kong was supported by RGC Hong Kong through 16303119 and N_HKUST608/17 and AoE/P-502/20. **Author contributions:** X.H., X.L., C.T.C., Q.S., S.W., and K.L. conceived the research. K.L., Y.Z., G.L., X.X.W., and C.D. contributed to the experiments. K.L., Z.D., and Y.Z. analyzed the experimental data. Z.D., K.L., and C.T.L. established the theoretical model. K.L., Y.Z., and Z.D. wrote the manuscript. K.L., Y.Z., Z.D., X.H., X.L., C.T.C., X.Y.W., and C.C.L. revised the manuscript. All the authors contributed to the preparation of the manuscript. X.H., X.L., C.T.C., Q.S., S.W., and Q.G. supervised the research. **Competing interests:** The authors declare that they have no competing interests. **Data and materials availability:** All data needed to evaluate the conclusions in the paper are present in the paper and/or the Supplementary Materials.

Submitted 15 October 2022
Accepted 13 March 2023
Published 12 April 2023
10.1126/sciadv.adf3470